

## ARTICLE OPEN



# The role of nano-sized intergranular phases on nickel alloy 725 brittle failure

Maria Sofia Hazarabedian<sup>1</sup> and Mariano Iannuzzi<sup>1</sup>✉

Although precipitation-hardened nickel alloys, such as Alloy 725, are extensively used in the most aggressive oil and gas production conditions given their a priori superior environmentally assisted cracking resistance, recent failures associated with hydrogen embrittlement (HE) cast doubts about their performance in H-bearing environments. These high-profile incidents have led to extensive research to elucidate the failure mechanism and develop methods to reduce risks. However, the microstructural features that made only specific heats of Alloy 725 susceptible to HE have yet to be agreed upon by the scientific community. Herein, our results showed that the abundant precipitation of F phase, i.e., a recently discovered nano-sized and embrittling phase, at grain boundaries increased cracking susceptibility. A continuous F phase network offered a low-energy path for crack opening by matrix-precipitate interfacial decohesion. Additionally, we correlated Alloy 725 microstructure with HE resistance, which is essential for thermomechanical processing optimization and the design of alternative qualification tests to obtain embrittlement-resistant nickel alloys.

*npj Materials Degradation* (2021)5:39; <https://doi.org/10.1038/s41529-021-00185-2>

## INTRODUCTION

In the oil and gas industry, precipitation hardening (PH) nickel alloys are commonly selected for applications that require high strength and toughness in highly corrosive environments<sup>1–5</sup>. Despite their superior mechanical and corrosion properties, components made of Alloy 716, 718, and 725 (Table 1) have failed in service in relatively benign conditions due to hydrogen embrittlement (HE)<sup>6–10</sup>. Most importantly, the documented failed Alloy 716 and 725 components complied with the relevant international standards<sup>1,6,7,11</sup>. Therefore, current best practices and control methods have been proven insufficient to detect compromised batches. These failures have led to extensive research by industry and academia in recent years, given the limited viable alternatives to PH nickel alloys for extreme oil and gas environments and the criticality of the components made of these materials<sup>2,12,13</sup>.

It is widely accepted that the causative factors promoting HE failures are a critical amount of diffusible hydrogen, tensile stresses (applied, residual, or both), and a material with a susceptible microstructure<sup>14</sup>. For instance, it is well established that Alloy 718 suffers a stark reduction in ductility by HE when a sufficient amount of  $\delta$  phase forms at grain boundaries (GBs), which occurs by the decohesion at the  $\delta$  phase/matrix interface<sup>9,10,15–17</sup>. However, for Alloy 725, there is no consensus on the microstructural features that promote HE susceptibility or how to produce resistant heats to reduce risks and prevent future failures<sup>2,11,18–21</sup>.

Currently, there are two leading hypotheses to explain the microstructural Alloy 725 HE susceptibility. The first line of research focuses on the GB character, while the second one concentrates on the role of intergranular precipitates. Researchers have studied the GB character of different Alloy 725 samples, showing that different GB types have different HE resistance and promote different crack initiation and propagation mechanisms<sup>18–22</sup>. Seita et al.<sup>20</sup> found that coherent twin boundaries (CTBs), also known as  $\Sigma 3$  boundaries terminated in {111} in reference to coincidence site lattice<sup>23,24</sup>,

were prone to crack initiation but had a low likelihood of further propagation. Crack initiation at twin boundaries in environments containing hydrogen was further supported by Zhang and coworkers<sup>25</sup>. The crack initiation susceptibility of CTBs was associated with plastic flow localization in the presence of hydrogen<sup>20,25</sup>, while the crack-reluctant propagation was linked to the low hydrogen solubility and high surface decohesion energy<sup>20,26,27</sup>. Nonetheless, recent experimental work on Alloy 716 evidenced hydrogen enrichment at CTBs on in-situ charged specimens (i.e., hydrogen was charged while the specimens were strained)<sup>28</sup>. Subsequently, Hanson et al.<sup>21</sup> concluded that GBs with low-index planes (BLIPs) were resistant to crack propagation as secondary cracks tended to arrested around them<sup>29</sup>. In some of these studies<sup>19,20</sup>, no evidence of segregation and precipitation at GB was found.

Although the GB character hypothesis can explain certain features of the observed Alloy 725 HE failures, an increasing number of works suggest that the presence of Cr- and Mo-rich GB precipitation drastically reduces HE resistance<sup>2,6,30–32</sup>. However, no convincing evidence has been provided to date to determine the role of intergranular phases on Alloy 725 HE field failures<sup>2,11,30</sup>. In the literature, these GB precipitates have been referred to as  $M_{23}C_6$  and  $\sigma$  phase, despite the fact that  $\sigma$  phase should not form at the temperature and time range that Alloy 725 is thermal treated<sup>1,30,33</sup>. Additionally, the effect of the intergranular phases on crack initiation and propagation has yet to be studied.

Iannuzzi et al.<sup>6</sup> studied the subsea failure of an Alloy 725 batch that presented a full GB decoration of a nanoscale Cr- and Mo-rich phase(s). Further research on the same failed batch unequivocally identified the intergranular phases as  $M_{23}C_6$  carbide and F phase, a nano-sized topologically close-packed (TCP) phase not previously reported in Alloy 725<sup>34</sup>. The crystal structure, chemical composition, and morphology of both precipitates were the focus of an earlier publication<sup>34</sup>. Brittle TCP phases such as F and  $\sigma$  phase are considered particularly detrimental as they affect mechanical properties, especially when they form intergranular

<sup>1</sup>Curtin Corrosion Centre, Curtin University, Perth, WA, Australia. ✉email: [Mariano.iannuzzi@curtin.edu.au](mailto:Mariano.iannuzzi@curtin.edu.au)

**Table 1.** Nominal chemical composition of common PH nickel alloys and the composition of the Alloy 725 failed component studied herein.

Material	Nominal Composition (wt. %)						
	Ni	Cr	Fe	Mo	Nb	Ti	Cu
Alloy 716 (UNS N07716) <sup>1</sup>	59–63	19–22	Bal.	7.0–9.5	2.75–4.0	1.0–1.6	0.23 max.
Alloy 718 (UNS N07718) <sup>1</sup>	50–55	17–21	Bal.	2.8–3.3	-	0.8–1.15	0.23 max.
Alloy 725 (UNS N07725) <sup>1</sup>	55–59	19–22.5	Bal.	7.0–9.5	2.7–4	1.0–1.7	-
Alloy 945X (UNS N09945) <sup>1</sup>	45–55	19.5–23	Bal.	3.0–4.0	2.5–4.5	0.5–2.5	1.5–3.0
Alloy 725 failed batch <sup>a</sup>	55.9	21.4	7.2	7.9	3.7	1.7	-

<sup>a</sup>The composition was established as the average of the seven randomly collected EDS spectra at 25 kV and a working distance of 15 mm.

as films or sheets<sup>35,36</sup>. F phase was notably more abundant than  $M_{23}C_6$  in the failed batch, while almost negligible in the other four random commercial batches studied<sup>34,37</sup>. Furthermore, F phase precipitated as 10–20 nm thick sheets in a continuous or discontinuous arrangement, while  $M_{23}C_6$  had a blocky morphology<sup>34,38</sup>.

The recently identified F phase precipitation in commercial Alloy 725 heats and its extensive GB coverage in the failed batch provided an excellent opportunity to investigate the role of GB precipitates on HE resistance. Thus, this investigation studied the role of the intergranular phases on crack propagation. The research focused on the failed component to identify microstructural features that facilitated cracking in normal service conditions. The characterization included (i) low- and high-resolution fractography, (ii) crack cross-section electron backscatter diffraction (EBSD) and GB precipitate occurrence, and (iii) transmission electron microscopy (TEM) study at the crack tip. Results supported the detrimental effect of continuous F phase precipitates and the crack growth mechanism. The findings are instrumental for the development of feasible approaches to mitigate HE susceptibility.

## RESULTS

### Cracking around intergranular precipitates

This investigation was conducted on an Alloy 725 seal used in subsea equipment that failed in service and was deemed susceptible to HE in a previous work<sup>6</sup>. Figure 1 illustrates the location of the main crack. Cracking occurred in both the radial and angular (circumferential) directions, initiating at suspected stress raisers and surrounding the component's perimeter. The seal was not directly exposed to cathodic protection, and no evidence of calcareous deposits was found (NB: calcareous deposit formation is an indirect indicator of a net cathodic polarization, which leads to hydrogen charging of subsea equipment<sup>39,40</sup>).

Figure 2 presents scanning electron microscope (SEM) images of the fracture surface of the failed seal. The fracture was fully intergranular with no evidence of plastic deformation (Fig. 2a). High-resolution images showed that the fracture surface was fully or partially covered by secondary phases (Fig. 2b–h). The characteristic morphologies of the two intergranular precipitates were identified, e.g., irregular and blocky for  $M_{23}C_6$  and continuous or discontinuous sheet for F phase (Fig. 2c, f, h)<sup>34</sup>. As a reference, the morphologies of intergranular precipitates in the bulk material are illustrated in Supplementary Fig. 1. In general, at each GB plane, the precipitates presented the same nature and morphology. Some grains, such as the one in Fig. 2d, were almost entirely covered by a continuous F phase network. Occasionally, parallel lines were observed on the fracture surface, linked to shadows produced by the thin precipitates (Fig. 2h).

Low kV energy-dispersive X-ray spectroscopy (EDS) in Fig. 3 supported the presence and identity of the intergranular precipitates on the fracture surface. Low kV EDS spectra were

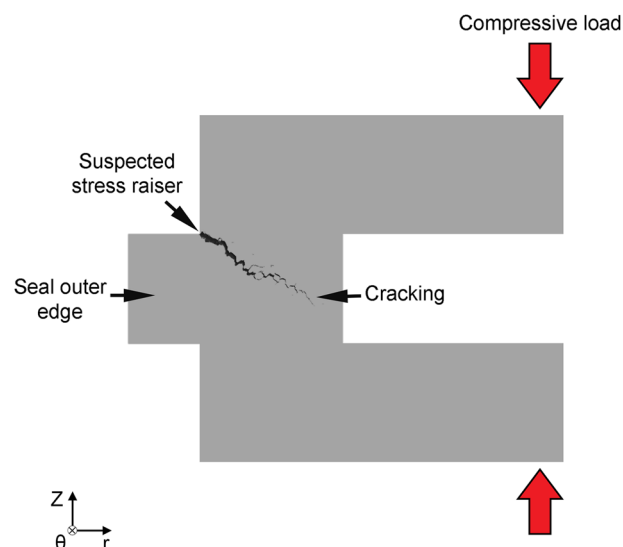


**Fig. 1** Failed component outer area cross-sectional view. Sketch illustrating a plausible stress concentration point and crack propagation direction.

acquired at positions 1–3 of Fig. 2c, which corresponded to (1)  $\gamma$ -matrix area free of intergranular precipitates, (2) a sheet-like precipitate (F phase), and (3) a blocky precipitate ( $M_{23}C_6$ ). Both intergranular precipitates presented a higher Cr content than the matrix (more evident on the blocky precipitate) and a lower Ni content. Moreover, the F phase sheet had a higher Mo content than the matrix and the blocky  $M_{23}C_6$  precipitate. These results were consistent with earlier scanning transmission electron microscopy (STEM)-EDS characterization of the F phase and  $M_{23}C_6$ <sup>34</sup>. TEM analysis of the crack tip cross-sections, such as the one presented in Fig. 4, supported the attachment of intergranular precipitates to the crack surface. In the TEM foil, intergranular precipitates were observed on both sides of the crack (Fig. 4). These precipitates were identified as hexagonal F phase by analyzing selected area diffraction (SAD) patterns acquired at  $[11\bar{2}]_F$  and  $[10\bar{1}0]_F$  zone axis (Fig. 4b, c)<sup>34,41,42</sup>. F phase precipitates were semicoherent with the left  $\gamma$ -matrix grain and presented the typical morphology previously characterized in the bulk material, i.e., flat and rounded interfaces with the semi-coherent (left) and incoherent (right)  $\gamma$ -matrix grains, respectively<sup>34</sup>. Generally, discontinuous precipitates were found attached to both surfaces of the crack. In contrast, longer precipitates tended to remain attached to the incoherent  $\gamma$ -matrix grain, such as the 4  $\mu$ m long continuous precipitate in Fig. 4.

The preserved morphology of the intergranular precipitates observed in the fracture surface by SEM and TEM suggested that the precipitates did not fracture during crack propagation. Therefore, the crack advanced by the interfacial decohesion

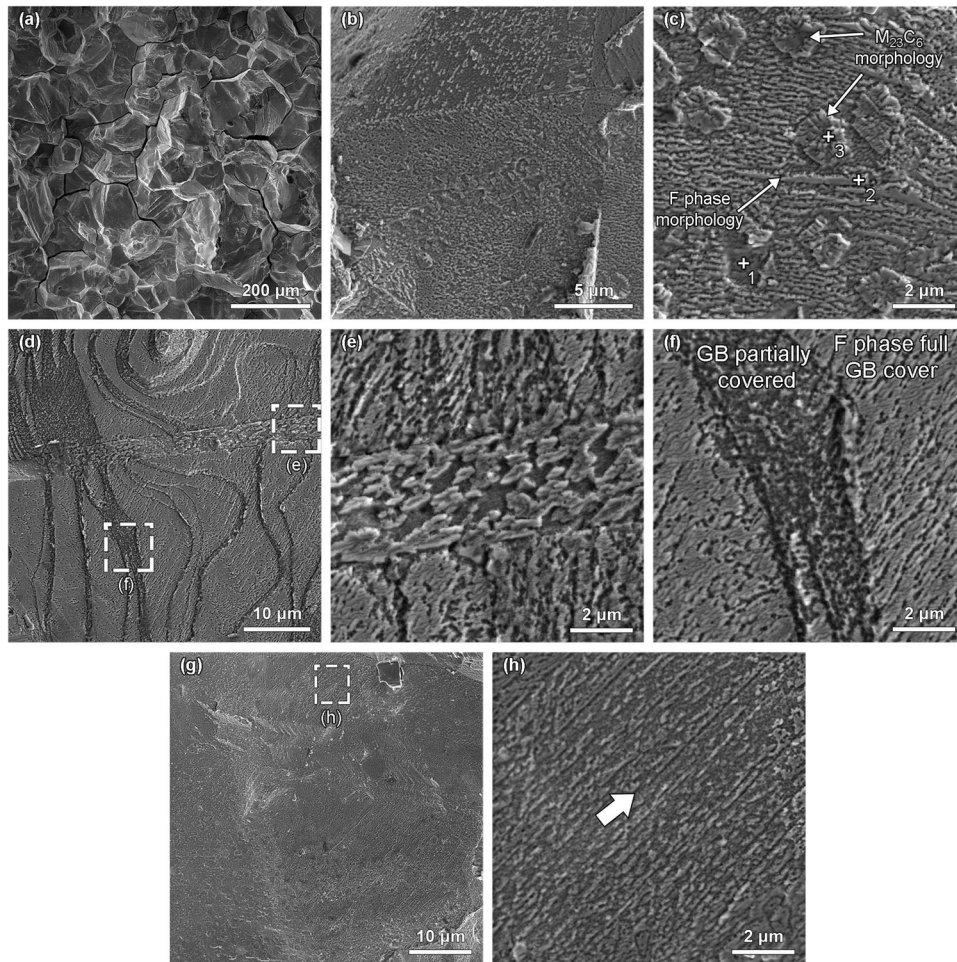


**Fig. 2 Fracture surface.** **a** Low magnification SEM images of fracture surface showing intergranular cleavage mode. **b–h** High-resolution SEM images showing intergranular precipitates covering the fracture surface. **c** Precipitates with the typical blocky and sheet-like morphologies of  $M_{23}C_6$  and F phase, respectively, as denoted in the image.

between the intergranular precipitate and the adjacent phase, i.e.,  $\gamma$ -matrix or  $\gamma'/\gamma''$  strengthening phases. In this regard, the earlier characterization on the failed batch suggested that F phase promoted the co-precipitation of Nb- and Ti-rich  $\gamma'/\gamma''$  phases<sup>34,38</sup>. Furthermore, no  $\gamma'/\gamma''$  precipitation free zone was observed around both F phase and  $M_{23}C_6$ , as assumed in another work on Alloy 725<sup>43</sup>. Interfacial decohesion of secondary phases during crack propagation has also been observed in other nickel alloys<sup>9,17,43,44</sup>. Additionally, for continuous precipitates, the crack tended to open along the flat precipitate and  $\gamma$ -matrix interface (Figs. 2f and 4a). In contrast, no preference was observed for discontinuous (shorter) precipitates.

### Barriers to crack propagation

The main crack cross-section of the failed component was studied to identify microstructural barriers for its propagation. Samples were characterized before and after revealing the intergranular precipitates by light optical microscopy and SEM (see “Methods”). EBSD was performed only before chemical etching since the as-polished surface condition improves the quality of the scans<sup>45</sup>. As the zero solutions of the EBSD scans did not overlap the crack, the crack shape adapted from the SEM images was superimposed to the EBSD maps to facilitate the analysis. The crack shape distortion was caused by sample tilting and drifting during the long EBSD data acquisition<sup>46</sup>.

Consistently with the fracture surface, the crack propagated intergranular and along high-angle GBs, which were predominant compared to low-angle GBs (Fig. 5b, c). According to the kernel average misorientation (KAM) map, there was not predominant  $\gamma$ -matrix misorientation near the crack; thus, the crack opened with almost no deformation of the  $\gamma$ -grains (Fig. 5d). Nonetheless, local plastic deformation was found following CTBs adjacent to the main crack (indicated by the arrow in Fig. 5d) and at crack arresting or inflexion points. In most cases, crack arrested or presented a discontinuous propagation at triple junctions or general GBs and CTB intersections.

Figure 6 compares the EBSD KAM map and the distribution of intergranular phases around the crack-tip shown in Fig. 5a. The KAM map in Fig. 6a has the crack shape superimposed in pink and the CTBs in white. Matrix deformation was observed when the crack propagation was discontinuous or when the crack arrested, as indicated by the arrows in Fig. 6a. Interestingly, according to the micrographs after etching, those deformation areas coincided with clean GB or, less commonly, a discontinuous network of intergranular precipitates (Fig. 6c, d, respectively). We corroborated that the discontinuous precipitation network in Fig. 6c was of discontinuous F phase by the TEM analysis of a foil extracted across the GB, shown in Supplementary Fig. 2. Additionally, SEM images showed intergranular precipitates within the crack (Fig. 6c, d). Finally, intergranular precipitates did not form at CTBs, as illustrated by comparing Fig. 6a, b.

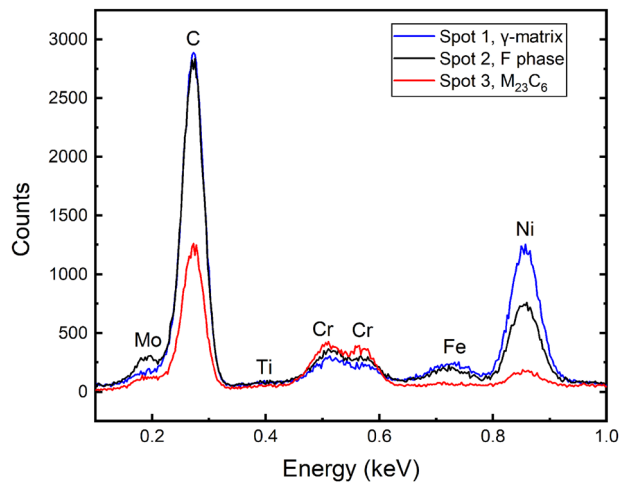


**Fig. 3 Low kV EDS on the fracture surface.** Point analyses were performed on the precipitates and matrix marked in Fig. 2c. Scan performed on a precipitate with F phase morphology was richer in Cr and Mo than the  $\gamma$ -matrix and presented less Ni. Likewise, the EDS spectrum collected on blocky precipitate was the richest on Cr and poorest on Ni, consistent with the  $M_{23}C_6$  composition. These EDS spectra are affected by both the chemical composition and the thickness of the precipitates. In this regard, given that F phase is typically 15 nm thick, the EDS scan would include a higher contribution of the sub-surface  $\gamma$ -matrix compared to the 100 nm thick  $M_{23}C_6$ . The carbon peaks should be disregarded as they result from unavoidable surface contamination. This EDS analysis correlates well with the one performed on Alloy 716 elsewhere<sup>28</sup>.

Figure 7 and Supplementary Table 1 summarize the statistical analysis of the crack arresting points. The crack arresting points were classified based on the presence of the intergranular phases (according to the optical micrographs) and the nature of the surrounding GBs, i.e., if the crack was connected to regular GBs or CTBs. Five types of arresting points were identified, as indicated in Fig. 7 and Supplementary Note. The count of each type was divided by the total of arresting points studied to calculate the fraction of each arresting point type. The probability of finding that type of junction in the baseline material was estimated according to Supplementary Note. The measured fraction of each type of arresting point and its probability to find the respective configuration of GBs in the base material are plotted in Fig. 7. Results showed that cracks arrested generally around clean GBs (Type 1 and 4). However, these types of junctions occurred less frequently in the baseline material microstructure. In contrast, the arresting points with adjacent intergranular precipitates (Type 3, 4, and 5) were uncommon, despite being more abundant in the base material. Therefore, results indicated that the decorated GBs offered low crack propagation resistance. The statistical significance of the detrimental effect of the decorated GBs was supported by  $P$ -values lower than  $2.5 \times 10^{-5}$  (Supplementary Note and Supplementary Table 1).

Supplementary Fig. 3 shows the only transgranular crack observed in this study. The crack propagated and arrested across a grain, introducing high strain. This crack was similarly orientated to a near CTB, according to the EBSD maps.

### The role of intergranular precipitation morphology on crack propagation

The preferential crack advance around continuous flat interfaces and the observed crack arrest at discontinuous precipitates (Figs. 2f, 4a, and 6c, respectively) suggested that the morphology of the intergranular precipitates played a role in crack propagation. Based on the evidence presented herein, we proposed a preferential crack propagation pathway surrounding the two

different F phase morphologies, illustrated in Fig. 8. For the discontinuous F phase precipitates, the crack path would be tortuous since it would be required to change direction to cross at least one of the interfaces of the adjacent grains (Fig. 8a). Additionally, considering the EBSD results shown in Fig. 6, clean GBs between the precipitates would locally deform before cracking, increasing the required energy for crack advance. Based on their morphology, crack growth around the blocky  $M_{23}C_6$  precipitates would be similar to that around the discontinuous F phase. However, the larger spacing between  $M_{23}C_6$  particles compared to the discontinuous F phase precipitates would result in higher strains (Supplementary Fig. 1a, b)<sup>34</sup>.

On the contrary, straight crack propagation can occur at the flat interface between the continuous F phase precipitate and the  $\gamma$ -matrix (Fig. 8b). Since the final crack path is shorter and results in no local matrix deformation, cracking around continuous precipitates would require less energy than around discontinuous ones. Furthermore, free crack paths favored by the continuous F phase precipitates would be in the  $\mu\text{m}$  range, as these precipitates were found to be as long as 45  $\mu\text{m}$  in the baseline material<sup>34</sup>.

### DISCUSSION

Previous research has proposed a mechanism to explain how cracking initiates in Alloy 725 in the presence of hydrogen<sup>20,25</sup>. In contrast, there is no clear consensus about plausible HE crack propagation mechanisms. In the failed component studied herein, we found that crack grew assisted by the interfacial decohesion of GB precipitates. Furthermore, results suggested that the morphology and distribution of the GB precipitate played a decisive role in the resulting crack advance resistance. In this regard, the continuous F phase would be the most favorable crack path, followed by the discontinuous F phase and then the blocky  $M_{23}C_6$  carbides. Thus, the HE susceptibility of the failed component was linked to the excessive intergranular precipitation dominated by F phase<sup>34,38</sup>, which offered minimal resistance to crack advance.

The high Mo content of F phase is another fact supporting its detrimental effect in Alloy 725<sup>34</sup>. As F phase is Mo-rich (Fig. 3) and Mo is a more efficient TCP former than Cr, its precipitation is favored in alloys with high Mo content<sup>34,47</sup>. Indeed, Alloys 716 and 725, which are the PH nickel alloys with the highest Mo content (Table 1), have been considered the most susceptible to HE<sup>1,16,30</sup>. In other words, PH nickel alloys with lower Mo content, such as Alloy 718 and 945X (Table 1), are less susceptible to GB formation of deleterious Mo-rich phases<sup>2</sup>. Likewise,  $\gamma'$  and  $\gamma''$  strengthening phases in PH nickel alloys also play a role in HE performance<sup>14,32,48</sup>. Hence, a direct comparison of Alloy 725 with alloy systems other than Alloy 716 should be done with caution since its intergranular precipitates, as well as the age-hardened matrix, would affect their behavior.

The more detrimental effect of F phase over  $M_{23}C_6$  is further supported by Aboura et al.<sup>28</sup>, who studied HE of Alloy 716. In their work, the enrichment of deuterium (i.e., an isotope of hydrogen) in several microstructural features, including intergranular precipitates, was determined on in-situ charged Alloy 716 specimens. The authors referred to the intergranular precipitates in Alloy 716 as discrete carbides or elongated  $\sigma$  phase based on previous works in related alloys. Nonetheless, their morphologies, composition, and backscatter electron images' contrast closely matched those of the  $M_{23}C_6$  and F phase identified in Alloy 725<sup>34</sup>. Aboura and co-workers found that the elongated precipitates (referred to as  $\sigma$  phase) directly accumulated deuterium, contrary to the carbides<sup>28</sup>. As the deuterium enrichment is associated with a higher hydrogen absorption capability, elongated precipitates would serve as preferred crack initiation sites and propagation paths<sup>17,28</sup>.

No crack advance through CTBs was found in the failed Alloy 725 component studied herein. On the contrary, CTBs delayed crack propagation as they led to the plastic deformation of the

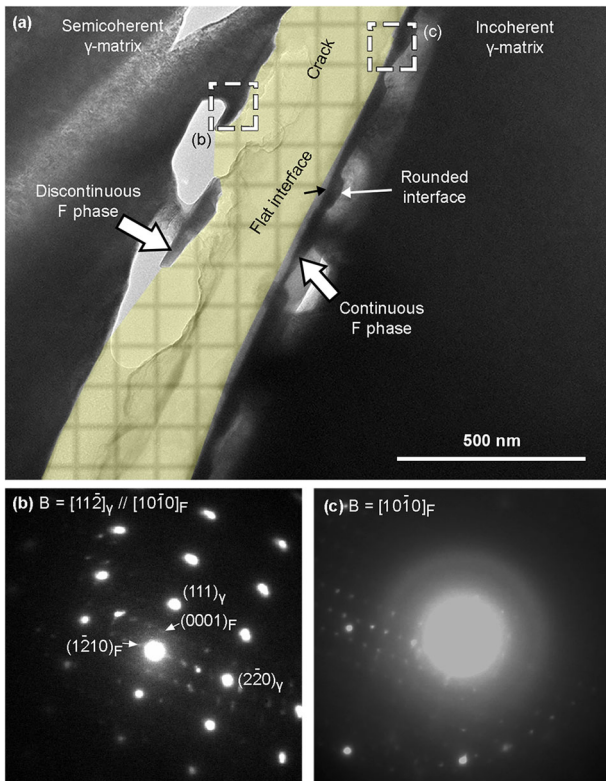


**Fig. 4 TEM crack tip cross-section.** **a** Bright field image, where the yellow area (NB: color added in post-processing to enhance the contrast) illustrates the crack path and the white arrows indicate F precipitates. The  $\gamma$ -matrix around the crack was partially milled out due to the difference in hardness between the  $\gamma$ -matrix and intergranular precipitates. This could not be avoided in the four samples extracted by FIB milling. Nonetheless, the intergranular precipitates were preserved and the crack propagation path was still evident (denoted in yellow in **(a)**). **b**, **c** SAD patterns obtained from the boxes marked on **(a)**, with the reflections of **(b)** F phase and the semicoherent  $\gamma$ -matrix on the left side of the crack and **(c)** F phase and the incoherent  $\gamma$ -matrix on the right side of the crack. None of the TEM specimens extracted along a crack from the failed seal presented  $M_{23}C_6$  carbide.

$\gamma$ -matrix (Fig. 5 and Supplementary Fig. 3), consistent with the descriptions in Seita et al.<sup>20</sup> and Aboura et al.<sup>28</sup> for Alloys 725 and 716, respectively. Although a crack close to a CTB was observed (Supplementary Fig. 3), the crack could not completely advance through it. The higher resistance of the CTBs compared to general GBs in Alloy 725 contrasted with what has been observed in Alloy 945X by Zhang and coworkers<sup>25</sup>, where cracks propagated through both types of boundaries. This difference in crack propagation resistance could be attributed to the Cr- and Mo-rich phases in Alloy 725's general GBs, which would serve as preferred crack propagation pathways over clean general GBs and CTBs (Fig. 6a, b)<sup>34</sup>. Secondary phase formation, such as F phase, is not expected at CTBs due to their low GB energy, which increases the activation energy barrier for heterogeneous nucleation<sup>49</sup>. Likewise, Alloy 945X's Mo content might be insufficient to form F phase at general GBs and therefore, general GBs and twin boundaries might have similar cracking resistances (Table 1)<sup>1,47</sup>. Additionally, no evidence of the void coalescence mechanism developed for Alloy 718 and previously applied to Alloy 725—e.g., dislocation slip bands (DSBs) at the fracture surface or the crack cross-section—was found in the failed Alloy 725 component<sup>27,31,43,50</sup>.

The brittle cracking observed in our work differs from another reported Alloy 725 HE failure, which presented ductile, cleavage, or mixed trans- and intergranular fracture<sup>7</sup>. In this regard,

although the authors suggested a purely cleavage transgranular failure mode, apparent intergranular cracking features were evident in the SEM images shown in the article. Contrastingly, the Alloy 725 failure studied herein shares many similarities with a reported failed Alloy 716 valve, such as brittle intergranular fracture mode, nano-sized intergranular precipitation, and crack propagation with negligible plastic deformation<sup>8</sup>.

A range of fracture modes has been described in both service-failed and laboratory Alloy 725 samples, as discussed above. Differences in failure modes may result from batch-to-batch differences in the availability of the plausible crack propagation paths, e.g., intergranular F phase and  $M_{23}C_6$  through interfacial decohesion or clean regions via void coalescence assisted by hydrogen accumulation in DSBs. In practice, cracks will open following the path with the lowest required energy, resulting in competition between the available mechanisms. This competitive behavior between propagation through intergranular precipitates and DSBs was evidenced in recent work on Alloy 716<sup>28</sup>. Similarly, earlier work on Alloy 725 showed that heats with a qualitatively determined greater extent of intergranular precipitates presented higher crack growth rate as well as predominant intergranular fracture<sup>43</sup>. In short, given that commercial Alloy 725 batches can have a broad range of F phase and  $M_{23}C_6$  precipitation in both extent and relative abundances, the nature, and extent of intergranular precipitation might affect not only HE resistance but also the prevailing mechanism. The processing conditions that promote the formation of one intergranular phase over the other are the focus of ongoing work.

The deleterious effect of intergranular F phase precipitation could be used to develop feasible approaches to detect susceptible microstructures and, thus, mitigate Alloy 725 HE risks. Firstly, it is strongly advisable to increase the impact toughness requirement suggested by the API 6ACRA standard<sup>1</sup>. In this regard, continuous intergranular precipitation in Alloy 718, 725, and 925 lowered absorbed impact energies by half when compared with control samples containing clean microstructures, which also resulted in a lower slow strain rate ratios<sup>51</sup>. Contrarily, other mechanical properties such as hardness and tensile strength showed no apparent trend with intergranular precipitation<sup>51</sup>. Secondly, the intergranular precipitates should be assessed by an objective methodology that is independent of the experience of the person conducting the test. In this regard, the double-loop electrochemical potentiokinetic reactivation (DL-EPR) test is commonly used to qualify other corrosion-resistant alloys and, as we showed elsewhere, has the potential to be introduced as a quality control method for Alloy 725<sup>37,38,52,53</sup>. The DL-EPR test was optimized to differentiate between the Alloy 725 failed microstructure studied herein and other commercial batches<sup>37,38</sup>. The sample preparation procedure for the DL-EPR technique is similar to that of the metallographic analysis required in API 6ACRA, takes around 1.5 h to perform, and quantifies the degree of sensitization (DOS), a value used to compare Alloy 725 heats. Both impact toughness and DOS are markedly affected by the extent of F phase and  $M_{23}C_6$  due to their brittle nature, morphology, and Cr- and Mo-depletion at the precipitate-matrix interface. Future work should focus on defining acceptance criteria, i.e., impact toughness and DOS requirements, based on the critical extent of both  $M_{23}C_6$  and F phase.

Future HE resistance studies should consider the extent and the predominant type of intergranular precipitates<sup>30,36</sup>. Herein, the effect of the morphology of the intergranular precipitates was discussed while other key factors in defining HE resistance, such as hydrogen diffusivity and trapping behavior of the GB phases, were not studied<sup>2,17,54</sup>. Moreover, current results are insufficient to estimate the maximum allowable F phase and  $M_{23}C_6$  content in service. Future work should focus on deconvoluting the influence of the nature of the GB precipitates

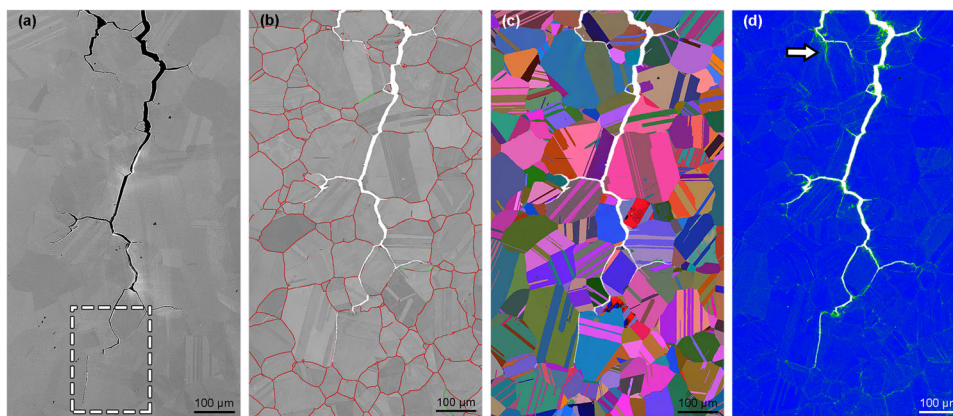


**Fig. 5 Crack cross-section analysis in the as-polished condition.** **a** SEM image. **b–d** EBSD maps with the crack shape overlapped in white. **b** Band contrast map with high and low angle regular GBs in red and green, respectively. **c** All Euler-angle map. **d** KAM map.

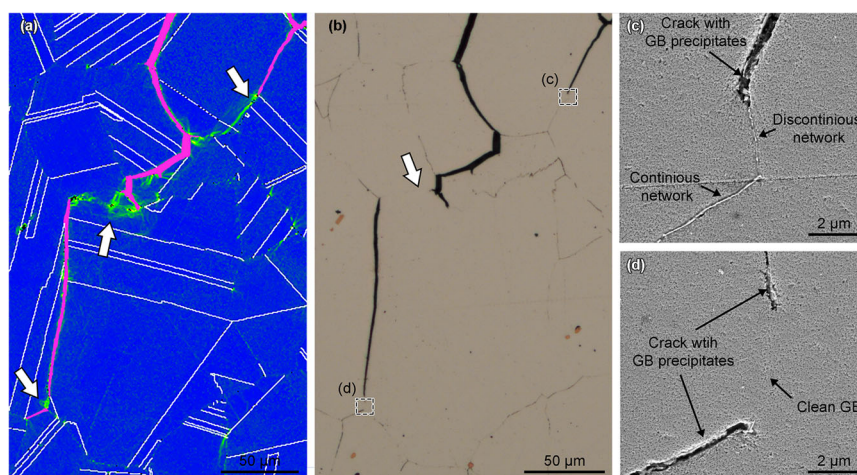


**Fig. 6 EBSD and intergranular precipitates occurrence analysis of crack tip.** Figure 6 analysis location is indicated in Fig. 5a. **a** KAM map indicating misorientation within the grains of the as-polished crack cross-section. **b** Optical micrographs and **c, d** SEM images of the occurrence of intergranular precipitates after chemical etching. Arrows and boxes indicate discontinuous propagation of the crack, which corresponded to clean or partially covered GBs and  $\gamma$ -matrix deformation.

on HE resistance to demonstrate their relative deleterious effect. Then, acceptance criteria should be defined based on HE performance. Additionally, a better understanding of the role of microstructure on HE resistance could be used to adjust thermomechanical processing parameters to minimize the level of deleterious GB phases by methods such as GB engineering<sup>2,55,56</sup>. Lastly, it is crucial to optimize HE test procedures for Alloy 725 to avoid excessively aggressive conditions<sup>10</sup>. Unfortunately, using test procedures optimized for Alloy 718 resulted in no apparent differences in performance between Alloy 725 heats, even if a failed field sample was included in the test matrix<sup>11,31,57,58</sup>.

In conclusion, the extensive and continuous GB network dominated by F phase precipitates in the failed Alloy 725 component degraded the cracking resistance of the material in service. Cracking occurred by decohesion of the intergranular precipitates and the  $\gamma$ -matrix/ $\gamma'$ - $\gamma''$  interface. Continuous F phase precipitates offered a straight,  $\mu\text{m}$ -long, and low-energy crack path. In contrast, clean GB and CTBs served as barriers for crack advance and led to the plastic deformation of the matrix. Quality control methods should be optimized to detect this type of susceptible microstructures and avoid potential incidents. A better understanding of the role of GB precipitates

gained in this investigation could be applied to develop heats of Alloy 725 with sufficient HE resistance for subsea service.

## METHODS

### Materials

The cracked seal used in this study was manufactured from a commercial Alloy 725 forged bar that was deemed susceptible to HE during oil and gas service (failed batch) (Table 1)<sup>6</sup>. The heat met the processing, mechanical properties, and microstructure requirements of the current API 6ACRA standard<sup>1</sup>. The extent and nature of the intergranular phases in the affected batch were previously studied<sup>34,38</sup>.

### Fractography

For cleaning the fracture surface, samples were immersed in dichloromethane in an ultrasonic bath, rinsed with acetone and deionized (DI)-water, and, finally, immersed in a 100 ml  $\text{H}_2\text{SO}_4$  and 900 ml DI-water solution in an ultrasonic bath<sup>59</sup>. The fracture surface morphology was studied with a field emission-scanning electron microscope (FE-SEM) equipped with an EDS detector with a 170  $\text{mm}^2$  sensor area. The elemental composition of the intergranular precipitates attached to the fracture surface was estimated by low kV EDS at 3 kV accelerating voltage and 10 mm working distance. Low kV EDS was employed to minimize the interaction volume of the technique and, thus, increase the spatial resolution and detect the intergranular precipitates that can be thinner than 10 nm<sup>34,60</sup>.

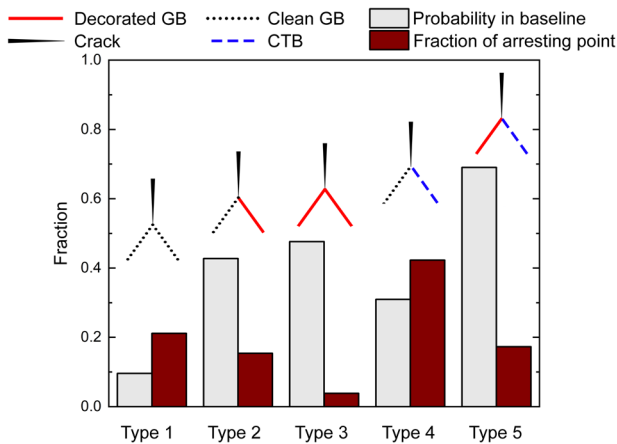


**Fig. 7 Statistical analysis of main crack arresting points.** The column chart shows, for each crack arresting point type, the measured fraction (red) along with the probability of that type GB junction in the baseline material (gray). The arresting points were classified based on the adjacent GBs' nature and decoration. Five categories were defined, depending on whether the crack tip was adjacent to (Type 1) two clean regular GBs, (Type 2) a clean and a decorated regular GBs, (Type 3) two decorated regular GBs, (Type 4) a clean regular GB and a CTB, and (Type 5) a decorated regular GB and a CTB.

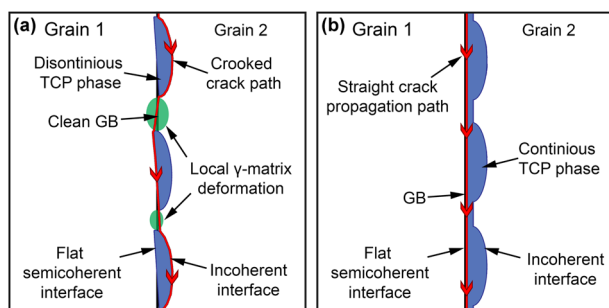


**Fig. 8 Proposed crack propagation pathway.** Cracking around (a) discontinuous and (b) continuous intergranular F phase precipitates.

### Crack cross-section analysis

Five cross-sections of the main crack were studied. The analysis involved (i) studying the crack propagation by SEM and EBSD, (ii) revealing the microstructure, and (iii) evaluating the occurrence of the intergranular precipitates by light optical microscopy and SEM. Samples exposing the main crack cross-section in the longitudinal–radial plane were mounted in cold-curing resin. The samples were polished down to 0.02  $\mu\text{m}$  using alumina suspension and carbon-coated. Light optical and SEM images, and EBSD maps were obtained in the as-polished condition using a FE-SEM equipped with an EBSD unit at 25 kV and a step size of 0.5  $\mu\text{m}$ . EBSD data was processed in the HKL Channel 5 software. Then, samples were polished with 1  $\mu\text{m}$  diamond suspension and etched by simple immersion in a 100 ml HCl (32 wt.%), 100 ml H<sub>2</sub>SO<sub>4</sub> (98 wt.%), and distilled water to make 1000 ml solution for 3 h to study the intergranular precipitation around the crack. The etching was developed to slightly dissolve the matrix to expose the GB precipitates without producing intergranular and pitting corrosion. Finally, the occurrence of intergranular precipitates was studied by optical microscopy and SEM at 5 kV. The superficial dissolution of the matrix is essential to correlate the etched micrographs with the as-polished analysis, and it was corroborated by the conservation of the crack and grain shapes before and after etching (Fig. 6). The statistical analysis of the different types of arresting points was performed according to Supplementary Note, adapted from Seita et al. approach<sup>20</sup>.

A set of TEM specimens was extracted close to the crack tip to study the precipitates within the crack. TEM specimens were prepared via focused-ion

beam (FIB) milling and the in-situ lift-out method<sup>61,62</sup>. The TEM characterization was performed using a commercial FE gun TEM operated at 200 kV. The identification of the phases and their coherency with the matrix were determined by manually analyzing SAD patterns.

### DATA AVAILABILITY

The data that support this investigation are available from the corresponding author on reasonable request.

Received: 1 May 2021; Accepted: 28 June 2021;

Published online: 19 July 2021

### REFERENCES

1. API 6ACRA. *Age-hardened Nickel-based Alloys for Oil and Gas Drilling and Production Equipment* (API, 2015).
2. Lu, X., Ma, Y. & Wang, D. On the hydrogen embrittlement behavior of nickel-based alloys: alloys 718 and 725. *Mater. Sci. Eng. A* **792**, 139785 (2020).
3. Mannan, S. K. Alloy 718 for oilfield applications. *JOM* **64**, 265–270 (2012).
4. Bhavsar, R. B., Collins, A. & Silverman, S. Use of alloy 718 and 725 in oil and gas industry. in *Superalloys 718, 625, 706 and Various Derivatives* 47–55 (TMS, 2001).
5. Onyewuenyi, O. Alloy 718-alloy optimization for applications in oil and gas production. in *Superalloy 718: Metallurgy and Applications* 345–362 (TMS, 1989).
6. Iannuzzi, M., Barnoush, A. & Johnsen, R. Materials and corrosion trends in offshore and subsea oil and gas production. *npj Mater. Degrad.* **1**, 2 (2017).
7. Shademan, S. S., Martin, J. W. & Davis, A. P. *UNS N07725 nickel alloy connection failure*. In *CORROSION 2012* Paper no. 1095 (NACE International, 2012).
8. Nice, P. et al. Hydrogen embrittlement failure of a precipitation hardened nickel alloy subsurface safety valve component installed in a North Sea seawater injection well. In *CORROSION 2014* Paper no. 3892 (NACE International, 2014).
9. Cassagne, T., Bonis, M. & Duret, C. Understanding field failures of alloy 718 forging materials in HP/HT wells. In *EUROCORR 2008* 1–13 (European Federation of Corrosion, 2008).
10. McCoy, S. A., Mannan, S. K., Tassen, C. S., Maitra, D. & Crum, J. R. Investigation of the effects of hydrogen on high strength precipitation hardened nickel alloys for O&G service. In *CORROSION 2015* (NACE International, 2015).
11. Duret-Thual, C. et al. Assessment of the hydrogen induced stress cracking resistance of precipitation hardened nickel-based alloys using the slow strain rate tensile test method—review of a three years test program. In *CORROSION 2019*, Paper no. 13284 (NACE International, 2019).
12. McCoy, S. A., Maitra, D., Mannan, S. K., Crum, J. R. & Tassen, C. S. The effect of hydrogen on plain and notched test specimens of precipitation hardenable nickel alloys. In *CORROSION 2017* Paper no. 9655 (NACE International, NACE, 2017).
13. Dodge, M., Sotoudeh, K., Gittos, M. & Griffiths, D. Hydrogen embrittlement of high strength precipitation hardenable nickel alloys. In *CORROSION 2019* p. 15 (NACE International, NACE, 2019).
14. Rebak, R. B. Environmentally assisted cracking of commercial Ni-Cr-Mo alloys—a review. In *CORROSION/2005 Conference* paper no. 5457 (NACE International, 2004).
15. Klöwer, J., Gosheva, O., Klapper, H. S. & Tarzimgohadam, Z. Effect of microstructural particularities on the corrosion resistance of nickel alloy UNS N07718—what really makes the difference? In *CORROSION 2017* (NACE International, 2017).
16. Morana, R., Smith, L. & Venkateswaran, S. P. On the susceptibility of precipitation hardened nickel alloys to hydrogen assisted cracking. In *CORROSION 2019* (NACE International, 2019).
17. Zhang, Z., Moore, K. L., McMahon, G., Morana, R. & Preuss, M. On the role of precipitates in hydrogen trapping and hydrogen embrittlement of a nickel-based superalloy. *Corros. Sci.* **146**, 58–69 (2019).
18. Stenerud, G., Johnsen, R. & Olsen, J. S. Hydrogen stress cracking and crack initiation in precipitation hardened Ni-alloys. *Eng. Fail. Anal.* **89**, 74–87 (2018).
19. Hanson, J. P., Seita, M., Jones, E., Gradečak, S. & Demkowicz, M. J. Hydrogen embrittlement behavior in precipitation hardened Ni-base alloys. In *CORROSION 2015* (NACE International, 2015).
20. Seita, M., Hanson, J. P., Gradečak, S. & Demkowicz, M. J. The dual role of coherent twin boundaries in hydrogen embrittlement. *Nat. Commun.* **6**, 6164 (2014).
21. Hanson, J. P. et al. Crystallographic character of grain boundaries resistant to hydrogen-assisted fracture in Ni-base alloy 725. *Nat. Commun.* **9**, 3386 (2018).
22. Lu, X. & Wang, D. Effect of hydrogen on deformation behavior of Alloy 725 revealed by in-situ bi-crystalline micropillar compression test. *J. Mater. Sci. Technol.* **67**, 243–253 (2020).
23. Humphreys, J., Rohrer, G. S. & Rollett, A. *Recrystallization and Related Annealing Phenomena* (Elsevier, 2017).

24. Rohrer, G. S., Randle, V., Kim, C. S. & Hu, Y. Changes in the five-parameter grain boundary character distribution in a brass brought about by iterative thermo-mechanical processing. *Acta Mater.* **54**, 4489–4502 (2006).
25. Zhang, Z. et al. Strain localisation and failure at twin-boundary complexes in nickel-based superalloys. *Nat. Commun.* **11**, 4890 (2020).
26. Chen, J. & Dongare, A. M. Role of grain boundary character on oxygen and hydrogen segregation-induced embrittlement in polycrystalline Ni. *J. Mater. Sci.* **52**, 30–45 (2017).
27. Zhang, Z., Obasi, G., Morana, R. & Preuss, M. Hydrogen assisted crack initiation and propagation in a nickel-based superalloy. *Acta Mater.* **113**, 272–283 (2016).
28. Aboura, Y., Martelo, D. F., Morana, R., Akid, R. & Moore, K. L. Characterising hydrogen induced cracking of alloy 625+ using correlative SEM-EDX and NanoSIMS. *Corros. Sci.* **181**, 109228 (2021).
29. Bagri, A. et al. Measuring grain boundary character distributions in Ni-base alloy 725 using high-energy diffraction microscopy. *Metall. Mater. Trans. A* **48**, 354–361 (2017).
30. Salvatori, I. et al. Assessment of the hydrogen induced stress cracking resistance of precipitation hardened nickel-based alloys using the slow strain rate tensile test method: influence of microstructure. In *CORROSION 2019* Paper no. 13365 (NACE International, 2019).
31. Li, X., Viswanathan, G. B. & Thodla, R. Hydrogen embrittlement study of two heats of UNS N07725 in sea water under cathodic polarization conditions. In *CORROSION 2020* Paper no. 15008 (NACE International, 2020).
32. Martelo, D. F., Morana, R. & Akid, R. Understanding the mechanical behaviour of 718 and 625+ nickel based super-alloys under cathodic polarization. *Theor. Appl. Fract. Mech.* **112**, 102871 (2021).
33. Mannan, S. & Veltry, F. Time-temperature-transformation diagram of alloy 725. In *Superalloys 718, 625, 706 and Various Derivatives* 345–356 (TMS, 2001).
34. Hazarabedian, M. S., Quadir, M. Z. & Iannuzzi, M. Characterization of intergranular phases in precipitation hardening Ni alloy UNS N07725. *Mater. Charact.* **171**, 110770 (2021).
35. Sabol, G. P. & Stickler, R. Microstructure of nickel-based superalloys. *Phys. Stat. Sol.* **35**, 11–52 (1969).
36. Wilson, A. S. Formation and effect of topologically close-packed phases in nickel-base superalloys. *Mater. Sci. Technol.* **33**, 1108–1118 (2017).
37. Hazarabedian, M. S., Quadir, M. Z. & Iannuzzi, M. Detecting intergranular phases in UNS N07725. Part II: Double-loop electrochemical potentiokinetic reactivation test validation. *J. Electrochem. Soc.* **168**, 031516 (2021).
38. Hazarabedian, M. S., Lison-Pick, M., Quadir, M. Z. & Iannuzzi, M. Detecting intergranular phases in UNS N07725. Part I: Adapting the double-loop electrochemical potentiokinetic reactivation test. *J. Electrochem. Soc.*, **168**, 031506 (2021).
39. Hazarabedian, M. S. et al. Hydrogen-induced stress cracking of swaged super duplex stainless steel subsea components. *CORROSION* **75**, 824–838 (2019).
40. Ou, K. C. & Wu, J. K. Effect of calcareous deposits formation on the hydrogen absorption of steel. *Mater. Chem. Phys.* **48**, 52–55 (1997).
41. Lin, Y. P. & Steeds, J. W. Identification of a hitherto unreported Frank–Kasper phase. *Acta Cryst.* **B42**, 159–162 (1986).
42. Li, D. X. & Kuo, K. H. Some new  $\sigma$ -related structures determined by high-resolution electron microscopy. *Acta Cryst.* **B42**, 152–159 (1986).
43. Ramgopal, T., Viswanathan, G. B., Amaya, H., Fahimi, B. & Taylor, C. D. Crack growth behavior of 725 in seawater under cathodic polarization. *Mater. Sci. Eng. A* **814**, 141112 (2021).
44. Shi, Q. et al. Fracture mode of a Ni-based single crystal superalloy containing topologically close-packed phases at ambient temperature. *Metall. Mater. Trans. A* **45A**, 1665–1669 (2014).
45. Nowell, M. M., Witt, R. A. & True, B. W. EBSD sample preparation: techniques, tips, and tricks. *Microsc. Microanal.* **11**, 504–505 (2005).
46. Winiarski, B. et al. Broad ion beam serial section tomography. *Ultramicroscopy* **172**, 52–64 (2017).
47. Kirby, G. N., Sponseller, D. L. & Van Vlack, L. H. The relative effects of chromium, molybdenum, and tungsten on the occurrence of  $\sigma$ -phase in Ni–Co–Cr alloys. *Metall. Trans.* **5**, 1477–1494 (1974).
48. Kernion, S. J., Magee, J. H., Werley, T. N. & Maxwell, P. *Offshore Technology Conference* (Offshore Technology Conference, 2014).
49. Porter, D. A. & Easterling, K. E. *Phase Transformations in Metals and Alloys* (Springer, 1992).
50. Zhang, Z., Obasi, G., Morana, R. & Preuss, M. In-situ observation of hydrogen induced crack initiation in a nickel-based superalloy. *Scr. Mater.* **140**, 40–44 (2017).
51. Mannan, S. & Puckett, B. Physical metallurgy of alloys 718, 925, 725, and 725SHS for service in aggressive corrosion environments. In *CORROSION 2003* Paper no. 03126 (NACE International, 2003).
52. International Organization for Standardization. *Petroleum, petrochemical, and natural gas industries—test methods for quality control of microstructure of ferritic/austenitic (duplex) stainless steels* (ISO 17781:2017). (2017).
53. Majidi, A. P. & Streicher, M. A. The double loop reactivation method for detecting sensitization in AISI 304 stainless steels. *CORROSION* **40**, 584–593 (1984).
54. Pound, B. G. Hydrogen trapping in precipitation-hardened alloys. *Acta Metall. Mater.* **38**, 2373–2381 (1990).
55. Bechtle, S., Kumar, M., Someday, B. P., Launey, M. E. & Ritchie, R. O. Grain-boundary engineering markedly reduces susceptibility to intergranular hydrogen embrittlement in metallic materials. *Acta Mater.* **57**, 4148–4157 (2009).
56. Palumbo, G. & Aust, K. T. Solute effects in grain boundary engineering. *Can. Metall. Q.* **34**, 165–173 (1995).
57. Trillo, E. et al. Assessment of the hydrogen induced stress cracking resistance of precipitation hardened nickel-based alloys using the slow strain rate tensile test method—experimental parameters and related issues. In *CORROSION 2019* Paper no. 13455 (NACE International, 2019).
58. Li, X., Viswanathan, G. B. & Thodla, R. Hydrogen embrittlement study of three heats of UNS N07718 in subsea applications. In *CORROSION 2019* (NACE International, 2019).
59. ASTM G 1–03. *Standard Practice for Preparing, Cleaning, and Evaluating Corrosion Test Specimens* (ASTM International, 2017).
60. Burgess, S., Sagar, J., Holland, J., Li, X. & Bauer, F. Ultra-low kV EDS—a new approach to improved spatial resolution, surface sensitivity, and light element compositional imaging and analysis in the SEM. *Microscopy Today* **25**, 20–29 (2017).
61. Tomus, D. & Ng, H. P. In situ lift-out dedicated techniques using FIB–SEM system for TEM specimen preparation. *Micron* **44**, 115–119 (2013).
62. Grabulov, A., Petrov, R. & Zandbergen, H. W. EBSD investigation of the crack initiation and TEM/FIB analyses of the microstructural changes around the cracks formed under rolling contact fatigue (RCF). *Int. J. Fatigue* **32**, 576–583 (2010).

## ACKNOWLEDGEMENTS

We acknowledge the support of Chevron, Woodside, and Roberto Rocca education program. Characterization was performed at the John de Laeter Center. We also thank Ms. Elaine Miller and Dr. Sam Bakhtiar for their assistance.

## AUTHOR CONTRIBUTIONS

M. S. H designed and performed the experiments, analyzed and discussed the results, and wrote and approved the paper; M. I. conceived the project, provided the materials, designed and supervised the experiments, discussed the results, and reviewed and approved the paper.

## COMPETING INTERESTS

The authors declare no competing interests.

## ADDITIONAL INFORMATION

**Supplementary information** The online version contains supplementary material available at <https://doi.org/10.1038/s41529-021-00185-2>.

**Correspondence** and requests for materials should be addressed to M.I.

**Reprints and permission information** is available at <http://www.nature.com/reprints>

**Publisher's note** Springer Nature remains neutral with regard to jurisdictional claims in published maps and institutional affiliations.



**Open Access** This article is licensed under a Creative Commons Attribution 4.0 International License, which permits use, sharing, adaptation, distribution and reproduction in any medium or format, as long as you give appropriate credit to the original author(s) and the source, provide a link to the Creative Commons license, and indicate if changes were made. The images or other third party material in this article are included in the article's Creative Commons license, unless indicated otherwise in a credit line to the material. If material is not included in the article's Creative Commons license and your intended use is not permitted by statutory regulation or exceeds the permitted use, you will need to obtain permission directly from the copyright holder. To view a copy of this license, visit <http://creativecommons.org/licenses/by/4.0/>.



